Instabilities of thermocapillary-buoyancy flow in a rotating annular pool for medium-Prandtl-number fluid

Hao Liu,[1,2] Jinchao He,[1,2] Zhong Zeng,[3] and Zhouhua Qiu[1,2,*]

[1]*Chongqing Southwest Research Institute for Water Transport Engineering, Chongqing Jiaotong University, Chongqing 400016, China*
[2]*Key Laboratory of Inland Waterway Regulation Engineering Ministry of Communications,*
Chongqing Jiaotong University, Chongqing 400074, China
and Chongqing Xike Consulting Center for Water Transport Engineering, Chongqing 400016, China
[3]*College of Aerospace Engineering, Chongqing University, Chongqing 400044, China*

(Received 22 April 2021; accepted 17 August 2021; published 1 September 2021)

The instabilities of the steady axisymmetric thermocapillary-buoyancy flow in a rotating annular pool were investigated by linear stability analysis. The critical instability parameters for the thermocapillary-buoyancy flow (normal gravity) and the pure thermocapillary flow (microgravity) were compared under different pool depths and rotation rates. The results show that the thermocapillary-buoyancy flow is more stable than the pure thermocapillary flow due to the stabilizing effect of the gravity (buoyancy) force. Two types of oscillatory instabilities were observed depending on the different rotation rates, and the propagation direction of the hydrothermal wave is also affected by the rotation rate.

DOI: 10.1103/PhysRevE.104.035101

I. INTRODUCTION

Thermocapillary flow, thermal-buoyancy flow, and rotating flow are important in many technical and industrial processes [1–4], for example, the Czochralski crystal growth, a widely used technique to grow large single crystals. During the Czochralski crystal growth, the thermocapillary force, buoyancy, and the rotation of the crystal and the crucible make the convection very complicated. The annular pool is a simplified model proposed to study the complex flow in the Czochralski growth, and therefore, the flow instability in rotating annular pools was extensively investigated in the past two decades.

Bauer and Eidel [5] theoretically studied the two-dimensional thermocapillary flow in a slowly rotating annular container. They considered two heating modes; one is the constant temperatures at the inner and outer walls, the other is time-oscillatory temperatures on the inner and outer walls, and the velocity distribution in the container was investigated. Subsequently, Sim and Zebib [6] numerically simulated the effect of rotation on oscillatory instability of thermocapillary flow of high-Prandtl-number fluid ($\mathrm{Pr} = 30$) in an open annulus. They reported that the rotation destabilized the flow, and the rotation parallel to the central axis of the annulus had a stronger influence than that perpendicular to the axis. By means of three-dimensional numerical simulations and linear stability analysis, Shi *et al.* [7,8] studied the influence of pool rotation on the thermocapillary flow in a shallow annular pool filled separately with silicone oil ($\mathrm{Pr} = 6.7$) and silicon melt ($\mathrm{Pr} = 0.011$). Similar to the results of Sim and Zebib [6], they also pointed out that the weak rotation destabilized the steady axisymmetric flow. In particular, for silicone oil the hydrothermal wave was found to propagate in the direction opposite to the pool rotation, while for silicon melt the hydrothermal wave propagated in the same direction as pool rotation. Moreover, Shi and Imaishi [9] also investigated the effect of the heating direction of the annular pool on the thermocapillary flow. With the three-dimensional numerical simulations, the effect of pool rotation on the thermocapillary flow of the silicon melt in a slowly rotating shallow annular pool was studied by Li *et al.* [10]. Two flow transitions, corresponding to two different hydrothermal waves, were observed with increasing the temperature difference. Corresponding to the numerical simulations of Li *et al.* [10], Yin *et al.* [11] further studied the effect of pool rotation on thermocapillary flow instabilities. Two shear instability mechanisms, caused by the thermocapillary force and pool rotation, respectively, were revealed by perturbation energy analysis. In particular, at a moderate rotation rate, the competition of the thermocapillary force and the pool rotation leads to three transitions between the steady axisymmetric flow and the three-dimensional oscillatory flow with the increase of Marangoni number. Recently, Li *et al.* [12] extended the work of Shi *et al.* [7] to a wider range of rotation rate and aspect ratio through linear stability analysis. Four types of hydrothermal wave instabilities were observed.

In the studies mentioned above, the buoyancy was neglected. In fact, in the process of Czochralski crystal growth, buoyancy also plays an important role, and the presence of buoyancy makes the flow more complicated. In order to well understand the instability of the thermocapillary-buoyancy flow in a rotating annular pool, a series of linear stability analyses was performed in this paper based on the spectral element method. In addition, the disturbance of the energy balance at the critical condition was calculated to reveal the underlying instability mechanism.

---

[*] Corresponding author: zhqiu@cqjtu.edu.cn

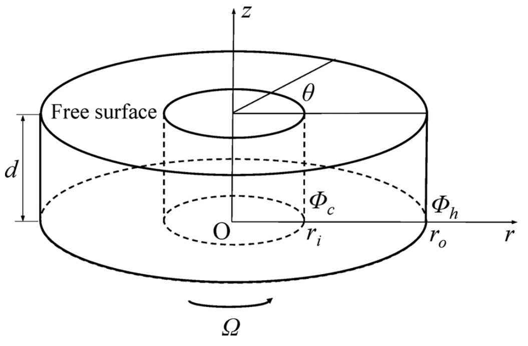

FIG. 1. Geometry of the annular pool.

II. PROBLEM DESCRIPTION AND NUMERICAL TECHNIQUES

A. Problem description and formulation

We consider an annular pool with the same geometry as in the space experiments of Schwabe *et al.* [13]. The inner radius r_i and outer radius r_o of the pool are 20 and 40 mm, respectively, and the depth d varies from 1 to 6 mm. The geometry of the annular pool is controlled by two parameters, namely, the aspect ratio $\Gamma = d/(r_o–r_i)$ and the radius ratio $\varepsilon = r_i/r_o$. The pool rotates around its central axis in the counterclockwise direction, which is defined as the positive azimuthal direction. The pool is heated from the outer wall and cooled from the inner wall, and the temperature of the outer and inner walls is maintained at Φ_h and Φ_c ($\Phi_h > \Phi_c$ and $\Delta\Phi = \Phi_h–\Phi_c$), respectively. In addition, the pool is filled with Li Ca Al F_6 melt and its physical properties refer to [14]. We introduce the following assumptions: (1) The bottom wall and the free surface are insulated. (2) The free surface is flat and nondeformable. (3) The surface tension on the free surface is a linearly decreasing function of temperature as $\sigma = \sigma_0–\gamma_T\Phi$, where σ_0 is the surface tension at the reference temperature Φ_c, and γ_T is the surface tension coefficient. (4) The Li Ca Al F_6 melt is regarded as an incompressible Newtonian fluid and the Boussinesq approximation is applied. (5) The no-slip condition is applied to all solid-liquid boundaries. (6) The inertial frame of reference is adopted, so the Coriolis force is not present in the equations. See Fig. 1.

Given the assumptions above, the dimensionless governing equations in the cylindrical coordinates are

$$\nabla \cdot \mathbf{u} = 0, \tag{1}$$

$$\frac{\partial \mathbf{u}}{\partial t} + (\mathbf{u} \cdot \nabla)\mathbf{u} = -\nabla p + \nabla^2 \mathbf{u} + \mathrm{Gr} T \mathbf{e_z}, \tag{2}$$

$$\frac{\partial T}{\partial t} + (\mathbf{u} \cdot \nabla) T = \frac{1}{\mathrm{Pr}} \nabla^2 T. \tag{3}$$

Here $\boldsymbol{u}$ is the nondimensional velocity vector, t the nondimensional time, and p the nondimensional pressure. The velocity, time, and pressure are nondimensionalized by $\nu/(r_o–r_i)$, $(r_o–r_i)^2/\nu$, and $\rho\nu^2/(r_o–r_i)^2$, respectively, where ν is the kinematic viscosity and ρ is the density. Moreover, the nondimensional temperature T is defined as $T = (\Phi–\Phi_c)/(\Phi_h–\Phi_c)$. Accordingly, the dimensionless parameters, $\mathrm{Gr} = g\beta\Delta\Phi(r_o–r_i)^3/\nu^2$ and $\mathrm{Pr} = \nu/\kappa$ are the Grashof and Prandtl numbers, respectively, where g is the gravitational acceleration, β is the thermal expansion coefficient, and κ is the thermal conductivity. The Prandtl number of Li Ca Al F_6 melt is 1.4.

The corresponding boundary conditions are as follows: the free surface ($z = \Gamma$),

$$\frac{\partial u}{\partial z} = -\frac{\mathrm{Ma}}{\mathrm{Pr}}\frac{\partial T}{\partial r}, \quad \frac{\partial v}{\partial z} = -\frac{\mathrm{Ma}}{\mathrm{Pr}}\frac{\partial T}{r\partial \theta}, \quad w = 0, \quad \frac{\partial T}{\partial z} = 0, \tag{4}$$

the bottom ($z = 0$),

$$u = 0, \quad v = \omega r, \quad w = 0, \quad \frac{\partial T}{\partial z} = 0, \tag{5}$$

the inner wall [$r = \varepsilon/(1–\varepsilon)$],

$$u = 0, \quad v = \omega r, \quad w = 0, \quad T = 0, \tag{6}$$

and the outer wall [$r = 1/(1–\varepsilon)$],

$$u = 0, \quad v = \omega r, \quad w = 0, \quad T = 1, \tag{7}$$

where u, v, and w are the velocity components in the radial, azimuthal, and axial directions, respectively. The dimensionless parameters, $\mathrm{Ma} = \gamma_T\Delta\Phi(r_o–r_i)/(\rho\nu\kappa)$ and $\omega = \Omega(r_o–r_i)^2/\nu$ are the Marangoni number and dimensionless rotational angular velocity, respectively, where Ω is the angular velocity of pool rotation.

B. Basic flow and disturbances

The system of Eqs. (1)–(7) admits an axisymmetric steady-state solution, which is the basis of linear stability analysis. The basic flow is firstly simulated by the spectral element method based on the time splitting method [11].

The linear stability of the basic flow is investigated by imposing the infinitesimal perturbations onto the basic flow:

$$(\mathbf{u}, p, T) = (\mathbf{u}_0, p_0, T_0) + (\hat{\mathbf{u}}, \hat{p}, \hat{T}). \tag{8}$$

Here $(\mathbf{u}_0, p_0, T_0)$ represents the basic flow, and $(\hat{\mathbf{u}}, \hat{p}, \hat{T})$ indicates the infinitesimal perturbation. Then the linearized perturbation equations are derived by substituting Eq. (8) into Eqs. (1)–(3) and neglecting the second-order infinitesimal,

$$\nabla \cdot \hat{\mathbf{u}} = 0, \tag{9}$$

$$\frac{\partial \hat{\mathbf{u}}}{\partial t} + (\mathbf{u}_0 \cdot \nabla)\hat{\mathbf{u}} + (\hat{\mathbf{u}} \cdot \nabla)\mathbf{u}_0 = -\nabla \hat{p} + \nabla^2 \hat{\mathbf{u}} + \mathrm{Gr}\hat{T}\mathbf{e_z}, \tag{10}$$

$$\frac{\partial \hat{T}}{\partial t} + (\mathbf{u}_0 \cdot \nabla)\hat{T} + (\hat{\mathbf{u}} \cdot \nabla)T_0 = \frac{1}{\mathrm{Pr}}\nabla^2 \hat{T}. \tag{11}$$

Similarly, the boundary conditions of the perturbations can be derived from Eqs. (4)–(7) as follows:

the free surface ($z = \Gamma$),

$$\frac{\partial \hat{u}}{\partial z} = -\frac{\mathrm{Ma}}{\mathrm{Pr}}\frac{\partial \hat{T}}{\partial r}, \quad \frac{\partial \hat{v}}{\partial z} = -\frac{\mathrm{Ma}}{\mathrm{Pr}}\frac{\partial \hat{T}}{r\partial \theta}, \quad \hat{w} = 0, \quad \frac{\partial \hat{T}}{\partial z} = 0, \tag{12}$$

the bottom ($z = 0$),

$$\hat{u} = \hat{v} = \hat{w} = \frac{\partial \hat{T}}{\partial z} = 0, \tag{13}$$

the inner wall $[r = \varepsilon/(1\text{–}\varepsilon)]$,

$$\hat{u} = \hat{v} = \hat{w} = \hat{T} = 0, \tag{14}$$

and the outer wall $[r = 1/(1\text{–}\varepsilon)]$,

$$\hat{u} = \hat{v} = \hat{w} = \hat{T} = 0. \tag{15}$$

We decompose the perturbations as the normal mode form, namely,

$$\begin{pmatrix} \hat{\mathbf{u}}(r,\theta,z,t) \\ \hat{p}(r,\theta,z,t) \\ \hat{T}(r,\theta,z,t) \end{pmatrix} = \begin{pmatrix} \tilde{\mathbf{u}}(r,z) \\ \tilde{p}(r,z) \\ \tilde{T}(r,z) \end{pmatrix} e^{(\lambda_r + i\lambda_i)t + ik\theta}. \tag{16}$$

Here λ_r and λ_i are the linear growth rate and the oscillation frequency, respectively, and k is the wave number in the azimuthal direction. Substituting Eq. (16) into Eqs. (9)–(15), a generalized eigenvalue problem is obtained as

$$\mathbf{A}\tilde{\mathbf{x}} = (\lambda_r + i\lambda_i)\mathbf{B}\tilde{\mathbf{x}}. \tag{17}$$

This generalized eigenvalue problem is solved using the Arnoldi algorithm from the ARPACK library [15]. The most dangerous mode is obtained by seeking the eigenvalue with the largest real part (λ_r), and the critical Marangoni numbers are determined from the condition $\lambda_{r\,\max} = 0$. Under the critical condition, the corresponding imaginary part (λ_i) of the eigenvalue is the critical oscillation frequency. In particular, $\lambda_i = 0$ indicates a stationary bifurcation while $\lambda_i \neq 0$ denotes an oscillatory (Hopf) bifurcation. After the oscillatory instability occurs, the angular velocity of oscillating wave is defined as $\omega_{osc} = -\lambda_i/k_c$. Therefore, $\lambda_i < 0$ represents that the oscillating wave propagates in the positive azimuthal direction (counterclockwise), the same as the pool rotation, while $\lambda_i > 0$ indicates that the oscillating wave propagates in the negative azimuthal direction (clockwise).

C. Energy analysis

In order to get some physical insights into the stability results, the disturbance energy analysis around the critical condition is performed. The total change rate of the disturbance kinetic energy (E_{kin}) is given by multiplying Eq. (10) with $\hat{\mathbf{u}}$ and integrating over the whole fluid region V, namely,

$$\frac{1}{D_k}\frac{dE_{\text{kin}}}{dt} = I_v + M_r + M_\theta + B_u - 1, \tag{18}$$

with the following terms:

the viscous dissipation of kinetic energy D_k,

$$D_k = \int_V (\nabla \times \hat{\mathbf{u}})^2 dV, \tag{19}$$

the interaction between the perturbation velocity and the basic flow I_v,

$$\begin{aligned} I_v &= I_{v1} + I_{v2} + I_{v3} + I_{v4} + I_{v5} + I_{v6} + I_{v7} + I_{v8} \\ &= \frac{1}{D_k}\int_V \bigg(-\hat{u}\hat{u}\frac{\partial u_0}{\partial r} - \hat{u}\hat{w}\frac{\partial u_0}{\partial z} + \frac{\hat{u}\hat{v}v_0}{r} - \hat{u}\hat{v}\frac{\partial v_0}{\partial r} \\ &\quad - \hat{v}\hat{w}\frac{\partial v_0}{\partial z} - \frac{\hat{v}\hat{v}u_0}{r} - \hat{u}\hat{w}\frac{\partial w_0}{\partial r} - \hat{w}\hat{w}\frac{\partial w_0}{\partial z}\bigg) dV, \end{aligned} \tag{20}$$

the work done by thermocapillary force on the free surface in the radial direction M_r,

$$M_r = \frac{1}{D_k}\int_S \left(\hat{u}\frac{\partial \hat{u}}{\partial z}\right) dS, \tag{21}$$

where S indicates the free surface,

the work done by thermocapillary force on the free surface in the azimuthal direction M_θ,

$$M_\theta = \frac{1}{D_k}\int_S \left(\hat{v}\frac{\partial \hat{v}}{\partial z}\right) dS, \tag{22}$$

and the work done by buoyancy force B_u,

$$B_u = \frac{\text{Gr}}{D_k}\int_V (\hat{T}\hat{w}) dV. \tag{23}$$

Similarly, the total change rate of the disturbance thermal energy is given by multiplying Eq. (11) with $\hat{T}$ and integrating over the whole fluid region,

$$\frac{1}{D_T}\frac{dE_T}{dt} = I_T - 1, \tag{24}$$

with the following terms:

the heat diffusion of the thermal energy D_T,

$$D_T = \frac{1}{\text{Pr}}\int_V (\nabla \hat{T})^2 dV, \tag{25}$$

and the convective transfer of thermal energy from the basic-state temperature field to the disturbance temperature field I_T,

$$I_T = I_{T1} + I_{T2} = \frac{1}{D_T}\left(-\int_V \hat{T}\hat{u}\frac{\partial T_0}{\partial r} dV - \int_V \hat{T}\hat{w}\frac{\partial T_0}{\partial z} dV\right). \tag{26}$$

The positive and negative values of the above energy terms indicate the destabilizing and stabilizing effect, respectively. In order to compare the disturbance energy balance under different parameters, the kinetic and thermal energy equations are normalized by the corresponding dissipation terms D_k and D_T, respectively.

III. NUMERICAL RESULTS AND DISCUSSION

The self-developed spectral element method codes for the basic state and the linear stability analysis had been validated in our previous papers [16,17]. The mesh convergence is also carefully checked and a nonuniform mesh $76^r \times 31^z$ (15 elements in the radial direction, six elements in the axial direction, and fifth-order discretization in both directions) is adopted in this paper. For the largest rotation rate calculated in this paper ($\omega = 250$), the relative deviation of the critical Marangoni numbers between the grids of fourth-, fifth-, and sixth-order discretization is less than 2%.

In order to evaluate the effect of gravity (buoyancy) force, we have considered two cases, namely, case A: normal gravity (1G) corresponding to the thermocapillary-buoyancy flow, and case B: zero gravity (0G) corresponding to the pure thermocapillary flow.

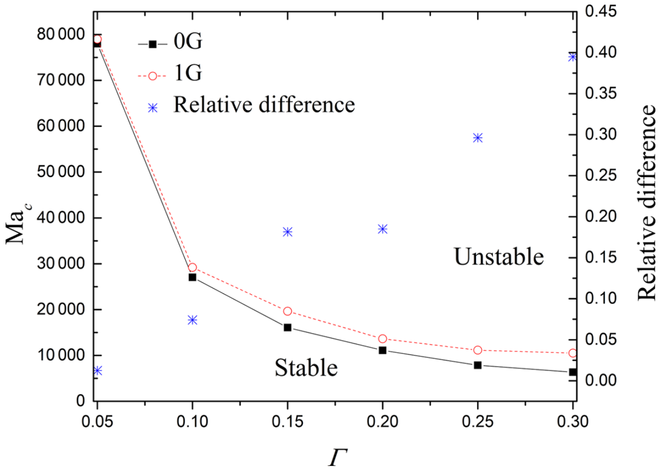

FIG. 2. Dependence of Ma_c and relative difference on the aspect ratio Γ ($\varepsilon = 0.5$, $\mathrm{Pr} = 1.4$, $\omega = 0$).

A. Comparison of the critical Marangoni numbers at different aspect ratios

Figure 2 shows the critical Marangoni numbers (Ma_c) for the thermocapillary-buoyancy flow and the pure thermocapillary flow versus the aspect ratio. The detailed critical parameters for different aspect ratios are listed in Table I in the Appendix. With the increase of aspect ratio, the critical Marangoni number decreases monotonically for both cases, while the relative difference of the critical Marangoni numbers increases. In the experiments conducted by Schwabe *et al.* [18], they reported that the gravity (buoyancy) is negligible when the liquid depth is less than 3 mm ($\Gamma = 0.15$). However, the present results show that even for a depth of 3 mm ($\Gamma = 0.15$), there is still a relative difference of about 18% between the two cases. Besides, we can see the thermocapillary-buoyancy flow is more stable than the pure thermocapillary flow; the reason will be explained in the subsequent section.

B. Effect of rotation on the flow instability

We adopt depth $d = 5$ mm ($\Gamma = 0.25$) to study the effect of rotation on the instability of thermocapillary and thermocapillary-buoyancy flow. The critical parameter values for the onset of flow instability under different dimensionless rotation rate ranging from $\omega = 0$ to 250 are determined, as listed in Table II in the Appendix. Figure 3 shows the dependence of the critical Marangoni number and oscillation frequency (f_c) on the rotation rate. As ω is increased, the Ma_c decreases slightly to a minimum of 7460 at $\omega = 12$ for 0G, and to a minimum of 11 102 at $\omega = 6$ for 1G. In other words, the weak rotation destabilizes the steady axisymmetric flow, and this result is consistent with that in earlier reports in the literature [7,10–12]. As ω is increased from this minimum, the Ma_c increases monotonically, and there is a transition of the instability mode when ω reaches a certain threshold value [see Fig. 3(a)]. This transition occurs at $\omega = 37$ for 0G, and at $\omega = 25$ for 1G. The f_c varies linearly with the increasing ω, and there is a jump change of f_c corresponding to the transition of the instability mode [see Fig. 3(b)].

TABLE I. Critical parameters for different aspect ratio Γ ($\varepsilon = 0.5$, $\mathrm{Pr} = 1.4$, $\omega = 0$).

Γ	Ma_c (0G)	f_c (0G)	k_c (0G)	Ma_c (1G)	f_c (1G)	k_c (1G)
0.05	77998	±4695.0	33	78984	±4665.7	32
0.10	27037	±1160.8	17	29202	±1211.4	17
0.15	16067	±530.3	12	19632	±574.4	16
0.20	11099	±303.3	11	13619	±314.2	10
0.25	7855	±193.1	9	11162	±214.4	8
0.30	6347	±138.8	8	10491	±167.6	7

TABLE II. Critical parameters for different rotation rate ω ($\Gamma = 0.25$, $\varepsilon = 0.5$, $\mathrm{Pr} = 1.4$).

ω	Ma_c (0G)	f_c (0G)	k_c (0G)	Ma_c (1G)	f_c (1G)	k_c (1G)
0	7855	±193.1	9	11162	±214.4	8
6	7531	127.7	9	11102	160.0	8
12	7460	63.2	9	11112	108.2	9
18	7617	–0.00234	9	11281	47.8	9
25	8104	–71.7	9	11734	–21.5	9
31	8805	–130.9	9	12285	–485.6	8
37	9747	–187.8	9	12378	–535.1	8
50	9750	–668.2	9	12400	–642.2	8
75	10140	–906.0	9	12741	–853.8	8
100	10818	–1144.0	9	13803	–1068.8	8
125	11719	–1382.7	9	15278	–1282.8	8
150	12839	–1621.9	9	17045	–1495.4	8
175	14156	–1861.5	9	19073	–1706.2	8
200	15635	–2101.1	9	21236	–1914.5	8
225	17252	–2340.6	9	23504	–2121.1	8
250	19164	–2580.3	9	25914	–2326.3	8

C. Instability mode and mechanism

1. *Instability of type I*

When the pool is not rotating, there will be a pair of conjugated critical oscillation frequencies with the same value and opposite signs. In other words, the hydrothermal wave propagates randomly in the positive or negative azimuthal direction with equal probability after the flow instability occurs. As ω is increased from zero, the critical oscillation frequencies decline linearly from the positive oscillation frequency of $\omega = 0$. The hydrothermal wave is clockwise (rotates in the direction opposite of the pool rotation) for $\omega < 18$ for 0G, and for $\omega < 23$ for 1G, and the hydrothermal wave is counterclockwise (rotates in the same direction as the pool rotation) for ω higher than these values, as shown in Fig. 4. A similar phenomenon is also reported by Feudel *et al.* [19] in the study of rotating waves in a rotating spherical shell.

Figure 4 shows that the disturbance temperature patterns on the free surface of instability type I are characterized by a series of curved spokelike waves. Compared with the pure thermocapillary flow, the thermocapillary-buoyancy flow has stronger disturbance temperature near the outer wall. The surface temperature patterns of instability type II will be presented in Fig. 8. The energy balances in Fig. 5 show that M_r, M_θ, and I_{v2} (secondary) are the main source of the

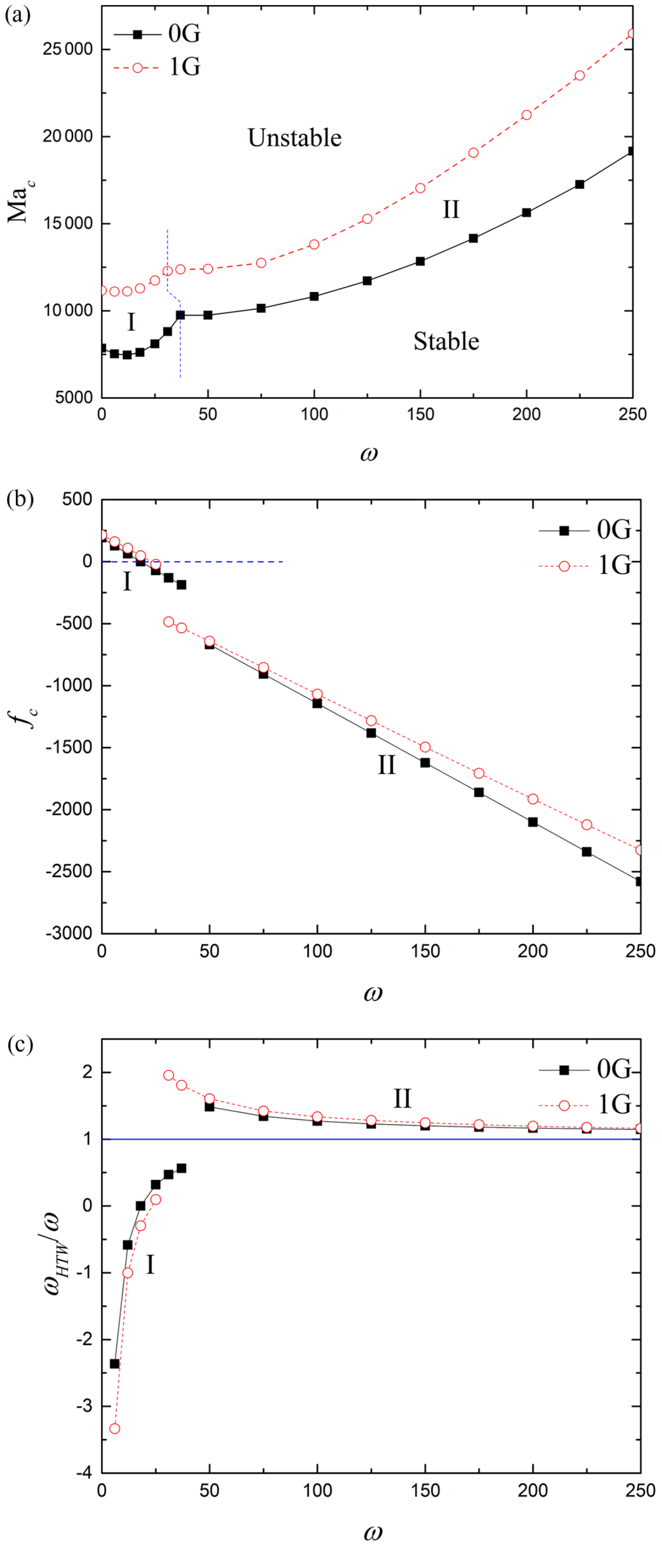

FIG. 3. Dependence of (a) Ma$_c$, (b) critical frequency f_c, and (c) $\omega_{\rm HTW}/\omega$ on the rotation rate ω ($\Gamma = 0.25$, $\varepsilon = 0.5$, Pr = 1.4).

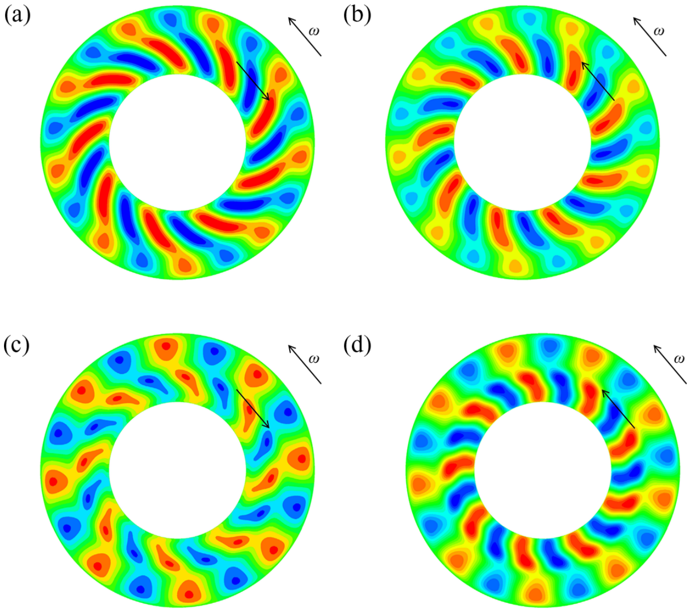

FIG. 4. Surface patterns of the perturbation temperature under the critical mode at (a) $\omega = 6$, $\Gamma = 0.25$, $\varepsilon = 0.5$, Pr = 1.4, Ma$_c$ = 7531 and (b) $\omega = 25$, $\Gamma = 0.25$, $\varepsilon = 0.5$, Pr = 1.4, Ma$_c$ = 8104 for pure thermocapillary flow. (c) $\omega = 6$, $\Gamma = 0.25$, $\varepsilon = 0.5$, Pr = 1.4, Ma$_c$ = 11 102; and (d) $\omega = 25$, $\Gamma = 0.25$, $\varepsilon = 0.5$, Pr = 1.4, Ma$_c$ = 11 734 for thermocapillary-buoyancy flow.

disturbance kinetic energy. Thus, the thermocapillary effect is the main cause for the flow instability. Moreover, we can see that B_u occupies a certain negative proportion, indicating a stabilizing effect of the buoyancy force. Therefore, the thermocapillary-buoyancy flow is more stable than the pure thermocapillary flow.

Since the flow instability is mainly caused by the thermocapillary mechanism, the analysis of the perturbation temperature field is the focus of discussion. From the thermal energy budget shown in Fig. 5, we can see both the radial transfer I_{T1} and axial transfer I_{T2} are responsible for the instability of the temperature field. For a deeper understanding of the heat transfer process, Figs. 6 and 7 show the basic-state field and critical mode under the critical condition. The quasi-two-dimensional stream function in Fig. 6 is calculated from the radial and axial velocities. It can be seen that there is a hot spot and a cold spot of temperature perturbation in the bulk, and the disturbance flow will transport thermal energy from the basic-state temperature gradient to the perturbation temperature field near the two spots.

2. *Instability of type II*

When the rotation rate ω is large enough, another type of hydrothermal wave arises and becomes the most dangerous instability mode. As shown in Fig. 3(b), the absolute value of the critical frequency f_c increases linearly with the increase of rotation rate ω. In order to further explain this linear relationship, Fig. 3(c) gives the dependence of $\omega_{\rm HTW}/\omega$ on the rotation rate ω, where $\omega_{\rm HTW} = -f_c/k_c$ is the angular velocity of hydrothermal wave propagation. We can see that $\omega_{\rm HTW}/\omega$ asymptotes to 1 when the rotation rate of the annular pool is large. This means that when the rotation rate is large, the propagation of the hydrothermal wave tends to be consistent with the rotation rhythm of the annular pool.

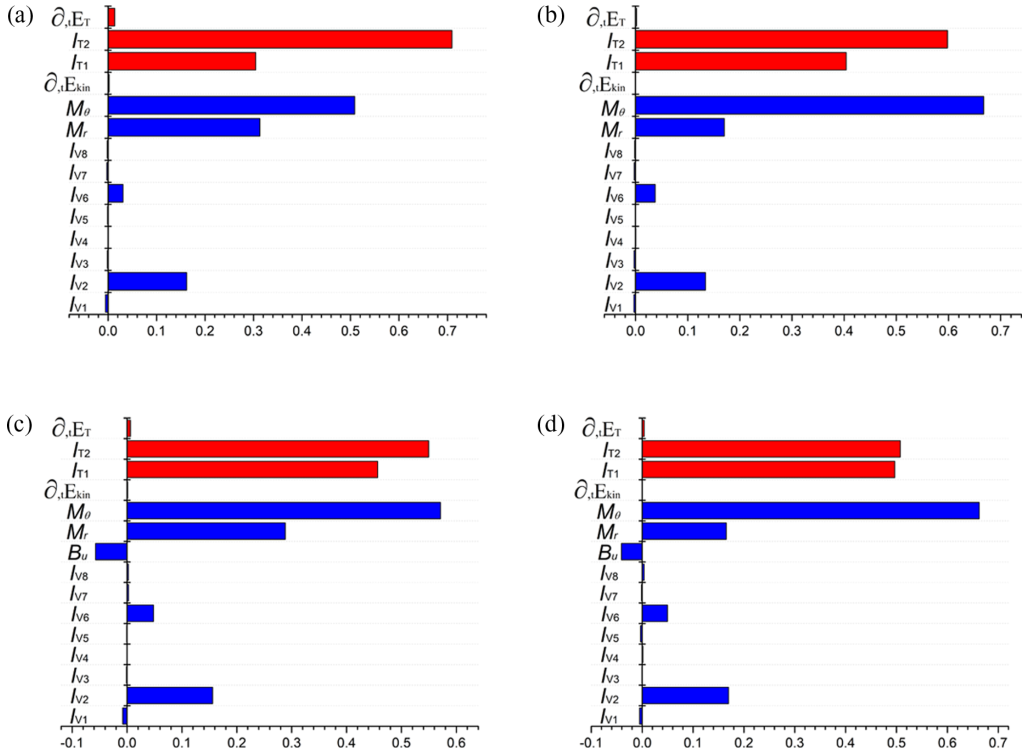

FIG. 5. Disturbance energy balance under the critical mode at (a) $\omega = 6$, $\Gamma = 0.25$, $\varepsilon = 0.5$, $\mathrm{Pr} = 1.4$, $\mathrm{Ma}_c = 7531$ and (b) $\omega = 25$, $\Gamma = 0.25$, $\varepsilon = 0.5$, $\mathrm{Pr} = 1.4$, $\mathrm{Ma}_c = 8104$ for pure thermocapillary flow. (c) $\omega = 6$, $\Gamma = 0.25$, $\varepsilon = 0.5$, $\mathrm{Pr} = 1.4$, $\mathrm{Ma}_c = 11\,102$ and (d) $\omega = 25$, $\Gamma = 0.25$, $\varepsilon = 0.5$, $\mathrm{Pr} = 1.4$, $\mathrm{Ma}_c = 11\,734$ for thermocapillary-buoyancy flow.

As demonstrated in Fig. 8, the surface patterns of the perturbation temperature take the form of parallelogramlike waves distributed near the outer (hot) wall. From Figs. 4 and 8 we can see that there are obvious differences between the

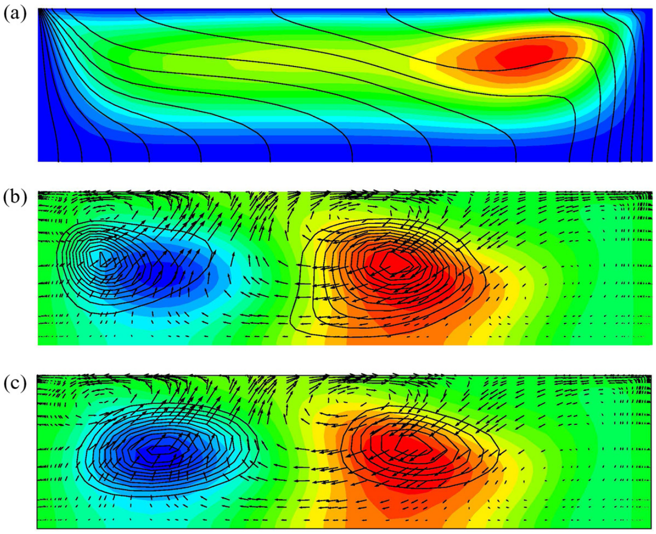

FIG. 6. Basic state and critical mode on a r-z cut plane where the perturbation temperature takes the maximum value for $\omega = 6$, $\Gamma = 0.25$, $\varepsilon = 0.5$, $\mathrm{Pr} = 1.4$, $\mathrm{Ma}_c = 7531$ under zero gravity. (a) Quasi-two-dimensional streamlines of the basic flow and distribution of the basic-state temperature T_0 (isolines). (b) Disturbance velocity vectors (arrows) and perturbation temperature combined with the local thermal energy i_{T1} (isolines). (c) Disturbance velocity vectors (arrows) and perturbation temperature combined with the local thermal energy i_{T2} (isolines).

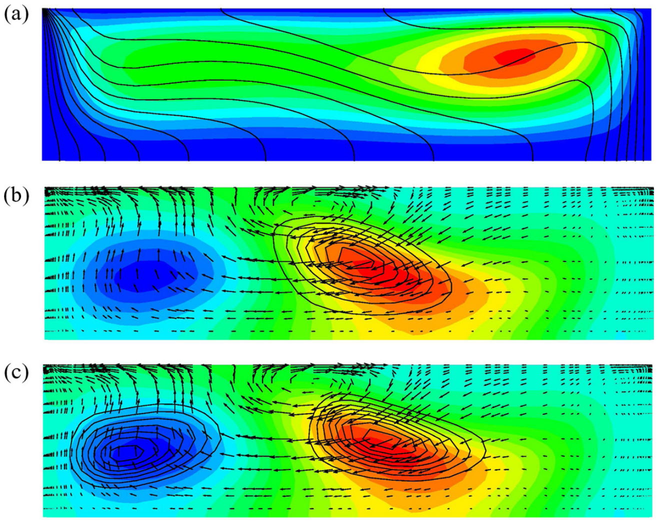

FIG. 7. Basic state and critical mode on a r-z cut plane where the perturbation temperature takes the maximum value for $\omega = 6$, $\Gamma = 0.25$, $\varepsilon = 0.5$, $\mathrm{Pr} = 1.4$, $\mathrm{Ma}_c = 11\,102$ under normal gravity. (a) Quasi-tw- dimensional streamlines of the basic flow and distribution of the basic-state temperature T_0 (isolines). (b) Disturbance velocity vectors (arrows) and perturbation temperature combined with the local thermal energy i_{T1} (isolines). (c) Disturbance velocity vectors (arrows) and perturbation temperature combined with the local thermal energy i_{T2} (isolines).

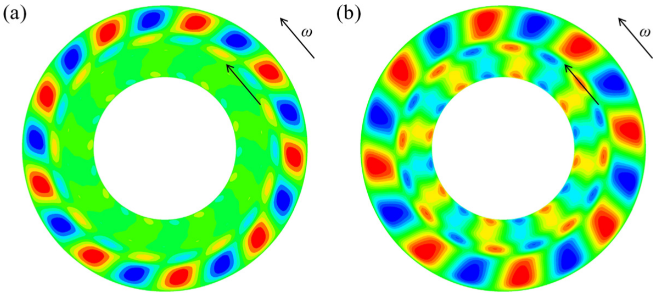

FIG. 8. Surface patterns of the perturbation temperature under the critical mode at (a) $\omega = 150$, $\Gamma = 0.25$, $\varepsilon = 0.5$, $\mathrm{Pr} = 1.4$, $\mathrm{Ma}_c = 12\,839$ for pure thermocapillary flow and (b) $\omega = 150$, $\Gamma = 0.25$, $\varepsilon = 0.5$, $\mathrm{Pr} = 1.4$, $\mathrm{Ma}_c = 17\,045$ for thermocapillary-buoyancy flow.

surface temperature pattern of instability type I and type II. The temperature perturbations of instability type II are more highly concentrated near the outer wall and are less curved (leaning but not spiraling) than those of type I. This surface temperature pattern is different from that of the typical hydrothermal wave, and it is also reported by Li *et al.* [12] in the study of thermocapillary flow in a rotating annular pool with medium Prandtl number ($\mathrm{Pr} = 6.7$). Moreover, from Table II we can see that for case 1G, the wave number changes from $k_c = 9$ to $k_c = 8$ at the transition of the instability mode. However, this change did not occur for case 0G. In fact, the wave number is related to the size of the instability cells [20]. The instability occupies a certain radial range, and the instability cells have approximately equal lengths in the radial and azimuthal directions. For instability type II, the instability for case 1G occupies a larger radial range than case 0G (see Fig. 8); therefore the instability cells for case 1G have larger length in the azimuthal direction than case 0G. Thereby, the wave number for case 1G is smaller.

The disturbance energy budget shows that M_r, M_θ, and I_{v2} (secondary) play the leading role in the energy balance (Fig. 9). It means that the thermocapillary effect is still the major cause of flow instability. Besides, we can see I_{v3}, I_{v4}, and I_{v5}, which are associated with the rotation, are very small compared with M_r and M_θ. Therefore, the pool rotation does not provide much additional energy for the flow instability, and its effect is reflected in the modification of the basic-state flow. In fact, the basic flow is of great significance in triggering this type of flow instability. Although the contributions of each energy term are similar to those of instability type I, the mechanisms are different. As shown in Figs. 10 and 11, there is only a hot spot of temperature perturbation in the bulk. Compared with the instability of type I, the cold spot near the inner (cold) wall disappears, resulting in the atypical surface patterns of perturbation temperature (see Fig. 8).

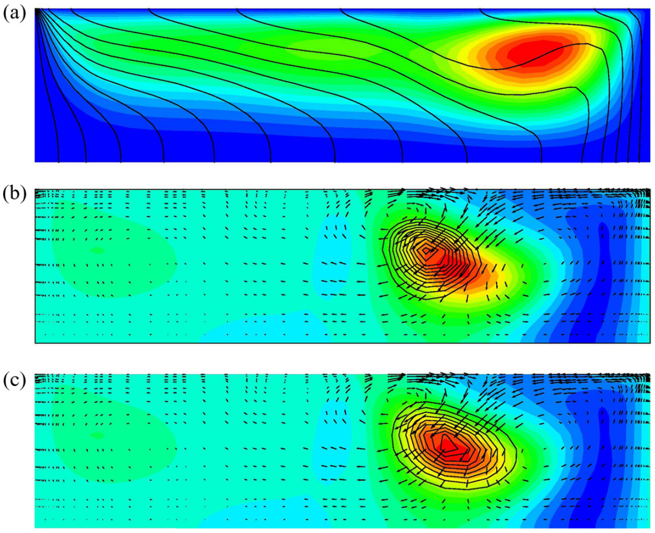

FIG. 10. Basic state and critical mode on a r-z cut plane where the perturbation temperature takes the maximum value for $\omega = 150$, $\Gamma = 0.25$, $\varepsilon = 0.5$, $\mathrm{Pr} = 1.4$, $\mathrm{Ma}_c = 12\,839$ under zero gravity. (a) Quasi-two-dimensional streamlines of the basic flow and distribution of the basic-state temperature T_0 (isolines). (b) Disturbance velocity vectors (arrows) and perturbation temperature combined with the local thermal energy i_{T1} (isolines). (c) Disturbance velocity vectors (arrows) and perturbation temperature combined with the local thermal energy i_{T2} (isolines).

IV. CONCLUSIONS

In this paper a series of linear stability analyses are performed to investigate the effect of rotation on the instabilities of thermocapillary and thermocapillary-buoyancy flow in annular pools. The results indicate that the ignoring of the

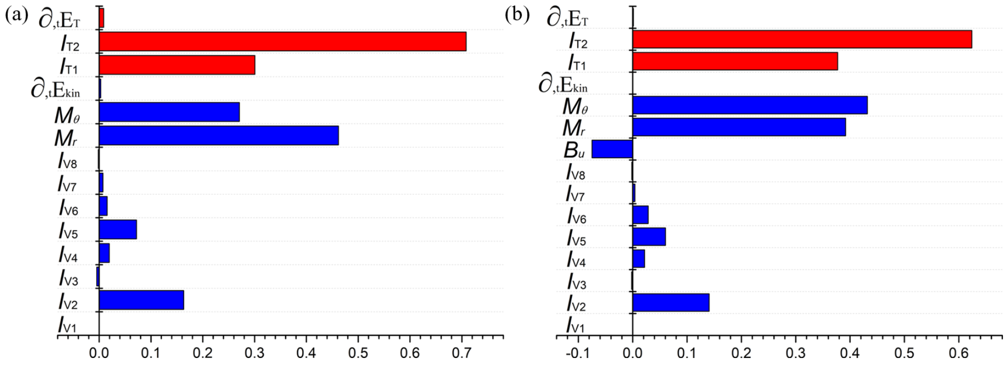

FIG. 9. Disturbance energy balance under the critical mode at (a) $\omega = 150$, $\Gamma = 0.25$, $\varepsilon = 0.5$, $\mathrm{Pr} = 1.4$, $\mathrm{Ma}_c = 12\,839$ for pure thermocapillary flow and (b) $\omega = 150$, $\Gamma = 0.25$, $\varepsilon = 0.5$, $\mathrm{Pr} = 1.4$, $\mathrm{Ma}_c = 17\,045$ for thermocapillary-buoyancy flow.

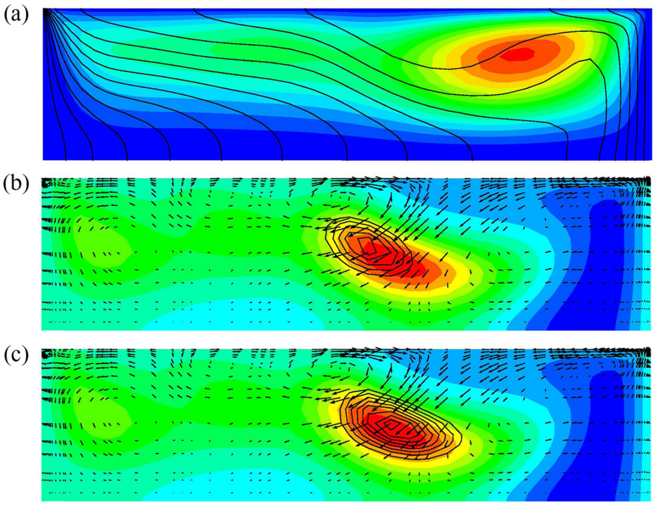

FIG. 11. Basic state and critical mode on a *r*-*z* cut plane where the perturbation temperature takes the maximum value for $\omega = 150$, $\Gamma = 0.25$, $\varepsilon = 0.5$, $\mathrm{Pr} = 1.4$, $\mathrm{Ma}_c = 17\,045$ under normal gravity. (a) Quasi-two-dimensional streamlines of the basic flow and distribution of the basic-state temperature T_0 (isolines). (b) Disturbance velocity vectors (arrows) and perturbation temperature combined with the local thermal energy i_{T1} (isolines). (c) Disturbance velocity vectors (arrows) and perturbation temperature combined with the local thermal energy i_{T2} (isolines).

buoyancy force would cause a large deviation even for the very small liquid depths, and the deviation increases with the increase of the liquid depth. The thermocapillary-buoyancy flow is more stable than the pure thermocapillary flow owing to the stabilizing effect of the buoyancy force.

For both thermocapillary-buoyancy flow and pure thermocapillary flow, the weak rotation destabilizes the flow while the strong rotation stabilizes the flow. Two types of flow instabilities are predicted. The first one occurs when the rotation rates are relatively small, and the hydrothermal wave propagates in the opposite or same direction of the pool rotation depending on the rotation rate. The second type of instability arises at relatively large rotation rates, and the hydrothermal wave propagates in the same direction as the pool rotation. The propagation velocity increases linearly as the rotation rate increases. The perturbation energy analysis indicates that the flow instability is mainly hydrothermal in nature. Although the pool rotation affects the critical instability parameters and the instability type, it does not provide a large amount of additional disturbance energy for the flow instability.

ACKNOWLEDGMENTS

This work is supported by the National Natural Science Foundation of China (Grant No. 11902142), and Chongqing Research Program of Basic Research and Frontier Technology (Grant No. cstc2015jcyjA00010).

APPENDIX

The critical instability parameters are shown in Tables I and II.

---

[1] O. Sánchez, I. Mercader, O. Batiste, and A. Alonso, Phys. Rev. E **93**, 063113 (2016).

[2] Y. Chao and Z. Ding, Phys. Rev. E **99**, 043101 (2019).

[3] L. Novi, J. von Hardenberg, D. W. Hughes, A. Provenzale, and E. A. Spiegel, Phys. Rev. E **99**, 053116 (2019).

[4] B. L. Smorodin, A. B. Mikishev, A. A. Nepomnyashchy, and B. I. Myznikova, Phys. Fluids **21**, 062102 (2009).

[5] H. Bauer and W. Eidel, Heat Mass Transfer **34**, 79 (1998).

[6] B.-C. Sim and A. Zebib, Phys. Fluids **14**, 225 (2002).

[7] W. Y. Shi, M. K. Ermakov, and N. Imaishi, J. Cryst. Growth **294**, 474 (2006).

[8] W. Y. Shi and N. Imaishi, Microgravity Sci. Technol. **19**, 159 (2007).

[9] W. Y. Shi and N. Imaishi, Microgravity Sci. Technol. **19**, 104 (2007).

[10] Y. R. Li, L. Xiao, S. Y. Wu, and N. Imaishi, Int. J. Heat Mass Transfer **51**, 1810 (2008).

[11] L. M. Yin, Z. Zeng, Z. H. Qiu, H. Mei, L. Q. Zhang, and Y. X. Zhang, Int. J. Heat Mass Transfer **97**, 353 (2016).

[12] H. M. Li, W. Y. Shi, and M. K. Ermakov, Int. J. Therm. Sci. **120**, 233 (2017).

[13] D. Schwabe, A. Zebib, and B.-C. Sim, J. Fluid Mech. **491**, 239 (2003).

[14] Z. Zeng, J. Chen, H. Mizuseki, K. Shimamura, T. Fukuda, and Y. Kawazoe, J. Cryst. Growth **252**, 538 (2003).

[15] R. B. Lehoucq, D. C. Sorensen, and C. Yang, *ARPACK Users' Guide: Solution of Large-Scale Eigenvalue Problems with Implicitly Restarted Arnoldi Methods* (SIAM, Philadelphia, 1998), Vol. 6.

[16] H. Liu, Z. Zeng, L. Yin, L. Qiao, and L. Zhang, Int. J. Heat Mass Transfer **127**, 996 (2018).

[17] H. Liu, Z. Zeng, L. Yin, Z. Qiu, and L. Qiao, Int. J. Therm. Sci. **137**, 500 (2019).

[18] D. Schwabe, U. Möller, J. Schneider, and A. Scharmann, Phys. Fluids A **4**, 2368 (1992).

[19] F. Feudel, N. Seehafer, L. S. Tuckerman, and M. Gellert, Phys. Rev. E **87**, 023021 (2013).

[20] Z. Zeng, H. Mizuseki, K. Shimamura, K. Higashino, T. Fukuda, and Y. Kawazoe, J. Cryst. Growth **229**, 601 (2001).